Available online at www.sciencedirect.com
ScienceDirect
Trans. Nonferrous Met. Soc. China 35(2025) 2386−2398
Transactions of Nonferrous Metals Society of China
www.tnmsc.cn

Electrolysis of Cu_2S into copper nanosheets and sulfur particles in ChCl−thiourea deep eutectic solvent

Ji-hua LI[1], Jin-feng ZHOU[1], Wei-jia CHEN[1], Shi-wei HE[1,2], Zhong-sheng HUA[1,2], Shi-liang CHEN[1], Hui KONG[1,3]

1. School of Metallurgical Engineering, Anhui University of Technology, Ma'anshan 243002, China;
2. Wuhu Technology and Innovation Research Institute, Anhui University of Technology, Wuhu 241000, China;
3. Anhui International Joint Research Center for Metallurgical Process and System Science, Ma'anshan 243002, China

Received 8 November 2023; accepted 26 June 2024

Abstract: Copper nanosheets and sulfur particles were synthesized synchronously by electrolysis, after dissolving Cu_2S in ChCl–thiourea (TU) deep eutectic solvent (DES) system. The optimized electrolysis conditions of 0.9 V, 80 °C, and 2 h resulted in the deposition of pure nano-sized copper sheets with a length of approximately 500 nm and a thickness of approximately 30 nm, and the production of sulfur particles with an average size of approximately 10 μm. The morphology of the cathodic products was significantly influenced by the electrolysis voltage. When Cu_2S was introduced into ChCl−TU, it dissolved $[CuCl_2]^-$ without disrupting the structure of the choline ion (Ch^+). As the electrolysis time increased, the copper deposition changed from wire to sheet growth, with the growth direction from radial to epitaxial along the substrate and back to radial.

Key words: cuprous sulfide; deep eutectic solvent; separation; cooper nanosheet; electro-recovery

1 Introduction

In the contemporary industrial landscape, sulfur dioxide (SO_2) emissions from sulfide metallurgy are the second highest, following those from coal-fired power plants [1]. Copper, the most abundant sulfurophilic metal, predominantly occurs as chalcocite (Cu_2S) and chalcopyrite ($CuFeS_2$) in the Earth's crust. Copper pyrometallurgy is the primary source of SO_2 emissions in the metallurgical industry. Moreover, metal extraction via hydrometallurgy in aqueous solutions can exacerbate environmental concerns by generating hydrogen (H_2) and SO_2. Therefore, there is a critical need for a more efficient and eco-friendly method for extracting Cu from sulfide ores to reduce their environmental impact. Among the various sulfur-containing smelting byproducts, pure monomeric sulfur is environmentally safe and ideal for smelting applications. Therefore, direct access to monomeric sulfur and metal monomers from sulfide metals through electrochemically facilitated oxidation and reduction processes is essential. The key aspect of this electrochemical process involves breaking the chemical bonds between the metal and sulfur, leading to the dissolution of sulfides in a suitable solvent [2].

Traditional aqueous solutions have a limited capacity to disrupt metal—sulfur bonds, hampering the dissolution of sulfide metals. Deep eutectic solvent (DES), an emerging class of green solvents composed of hydrogen bond donors and quaternary ammonium salts, exhibits low melting points and high stability, biodegradability, recyclability, and environmental friendliness [3]. Researchers have

Corresponding author: Shi-wei HE, Tel/Fax: +86-555-2311571, E-mail: heshiweiahut@163.com;
Hui KONG, E-mail: konghui@ahut.edu.cn
https://doi.org/10.1016/S1003-6326(25)66822-1

shown that DESs are highly soluble in metal sulfides because of their strong complexing abilities [4]. Numerous studies have confirmed that various metal ions, including Zn [5], Ni [6], Ag [7], Al [8], Mg [9], and Cr [10], can be electrochemically reduced in DES. Therefore, dissolving sulfide metals in DES and utilizing electrochemical methods to drive the oxidation and reduction reactions offer a promising avenue for producing monomeric sulfur and metal monomers while minimizing the environmental impact. For instance, LIU et al [11] successfully dissolved ZnO in urea and 1-butyl-3-methylimidazolium chloride (BMIC) ionic liquid to obtain metallic Zn through electrochemical reduction at the cathode. Similarly, YANG and REDDY [12] achieved the reduction of Zn metal from ZnO dissolved in a choline chloride (ChCl)−urea DES, observing that the metal oxide dissolved in a complex anion state in the DES. TANG et al [13] dissolved SnO in a solution containing 1-butyl-3-methylimidazole sulfate in a small amount of water and obtained metallic Sn via electrochemical reduction on a Cu-based cathode. Moreover, the addition of water increases the amount of singlet Sn on the cathode. PbO can be dissolved in urea−BMIC or ChCl−urea DES and subsequently reduced at the cathode to obtain metallic Pb with varying morphologies [14,15]. CuO can be dissolved in ChCl−urea/glycol DES, and Cu metal can be obtained through constant potential electrolysis, resulting in a more uniform microscopic morphology of the Cu deposition layer in ChCl−urea DES [16].

Sulfur and oxygen belong to the same group of elements and certain DESs exhibit high solubilities in metal sulfides. ABBOT et al [17] conducted research on the dissolution of pyrite in ChCl−glycol DES, achieving mineral dissolution and element recovery via electrochemical methods. WANG et al [18] reported the direct electrochemical reduction of Sb_2S_3 in a ChCl−glycol DES to prepare Sb powder and nano-sulfur. This opens a new pathway for environmentally friendly metal extraction from sulfide ores using DES, operating at near-room temperature and offering a concise process without SO_2 emissions. WANG et al [19] successfully desulfurized Cu_2S and recovered Cu in a ChCl−glycol DES, obtaining pure polycrystalline nano-Cu with an average size of approximately 16.15 nm. Nevertheless, reports on the electrochemical recovery of metal sulfides from DES are scarce, and the simultaneous recovery of Cu and S through electrochemical methods after sulfide dissolution in DES remains unexplored.

Recently, it was reported that thiourea plays a special role in metal electrolysis. GUO et al [20] reported that thiourea contributed to the formation of specialized microstructures of the deposited Mn and could modify the nucleation and growth model of Mn nuclei and accelerate the generation of homogeneous nuclei with a significantly enhanced nucleation rate. WANG et al [21] reported that metal oxides were more soluble in thiourea-based DESs. Owing to its enhanced coordination capacity as a hydrogen-bond donor, thiourea exhibits a superior ability compared to urea to capture and release protons as a hydrogen-bond acceptor in optimal circumstances. CHEN et al [22] reported that ChCl−TU provided an in situ sulfur source in addition to acting as a solvent and played a structure-controlling role in the formation of nanostructures with tint nanoparticles as subunits.

In this study, ChCl–TU DES was employed to solubilize Cu_2S, and Cu nanosheets and sulfur particles were obtained at the cathode and anode, respectively, through electrolysis. The electrochemical behavior of Cu and S before and after Cu_2S dissolution in ChCl−TU was investigated and the reaction mechanism of Cu_2S in ChCl−TU was discussed. To the best of our knowledge, this is the first time that nanosheet-structured Cu deposits have been synthesized using ChCl–TU. This study provides a novel perspective on the direct separation and recovery of Cu and S from Cu_2S, enriching the electrochemical theory of metallic compounds with oxygen groups in DES.

2 Experimental

2.1 Materials

All chemical reagents, choline chloride (ChCl) [$HOC_2H_4N(CH_3)_3Cl$] (Macklin, analytical grade ≥98%), thiourea (TU) [NH_2CSNH_2] (SCR, analytical grade 98%) and Cu_2S (Macklin, 99%), were used as acquired without further purification.

2.2 Preparation of deep eutectic solvent

A eutectic mixture was prepared using 1 mol

of ChCl (quaternary ammonium salt) and 2 mol of TU (hydrogen bond donor species) at 80 °C until the formation of a colorless and uniform liquid. ChCl and TU were dried at 343 K for 24 h in a vacuum oven. For the electrodeposition, solutions were prepared by dissolving 0.02 mol/L of Cu_2S in the eutectic mixture. Figure 1 shows a schematic of Cu dissolution in ChCl−TU. The experimental temperature of 80 °C was selected owing to the favorable viscosity and conductivity of the electrolyte at this temperature.

2.3 Electrochemical measurements

Cyclic voltammetry (CV) measurements were performed in a three-electrode system using an electrochemical workstation (PGSTAT 302N, Metrohm Autolab, Switzerland). A disk electrode made of platinum wrapped in polytetrafluoro-ethylene was used as the working electrode, and the working area of the platinum was 0.1257 cm^2. Ag/AgCl and graphite were used as the reference and counter electrodes, respectively. The scan range of cyclic voltammograms was from the initial potential of 2.2 V (vs Ag/AgCl) to the final potential of −2.0 V (vs Ag/AgCl) at 50 mV/s and 80 °C. Before each experiment, the surface of the working electrode was polished to a specular finish with 5000-grit sandpaper to prevent the influence of the last experiment on the new test. The working electrode was washed with deionized water and then cleaned and dried by ultrasound. The electrochemically active surface areas (ECSAs) before and after deposition were indirectly obtained using the electrochemical double-layer capacitance (C_{dl}). The C_{dl} was determined from cyclic voltammograms at a non-Faradaic potential region range from −0.47 to −0.42 V (vs MOE) with different can rates (from 160 to 20 mV/s) in 1 mol/L KOH electrolyte. The ECSA can then be obtained using the C_{dl} according to the equation: ECSA=C_{dl}/C_s, where C_s is a specific capacitance value of 0.04 mF/cm^2 in 1 mol/L KOH solution.

2.4 Electrolysis experiments

Before examining the deposition, the cell voltage of the electrolyte was measured using a three-electrode system and a DC power supply (HLR−7530D). The cathode consisted of a stainless steel sheet with an effective area of 1 cm × 1 cm, with graphite serving as the anode. The immersion depth of the cathode in the liquid and the distance between the electrodes were both maintained at 1 cm. Before the experiment, all electrodes were rinsed with deionized water and absolute ethanol and then dried in a vacuum drying oven for later use, especially for the cathode that needed to be polished to remove the surface oxide layer.

2.5 Characterization

The structures of ChCl−TU with and without Cu_2S were analyzed using Fourier-transform infrared (FT-IR) spectroscopy (Nicolet iS 10) and electrospray ionization mass spectrometry (ESI-MS, Thermo Scientific Q Exactive). The morphologies and elemental compositions of the products were characterized using a scanning electron microscope (SEM, Navo NanoSEM450) equipped with an energy-dispersive spectrometer (EDS, AZtecOne X-Max20). The phases of the products were analyzed by X-ray diffraction (XRD, Rigaku D/Max−2550) at a scan rate of 10 (°)/min in the range of 2θ=20°−100°. The X-ray photoelectron spectroscopy (XPS, Thermo Nexsa) was used to determine the elemental compositions of the samples.

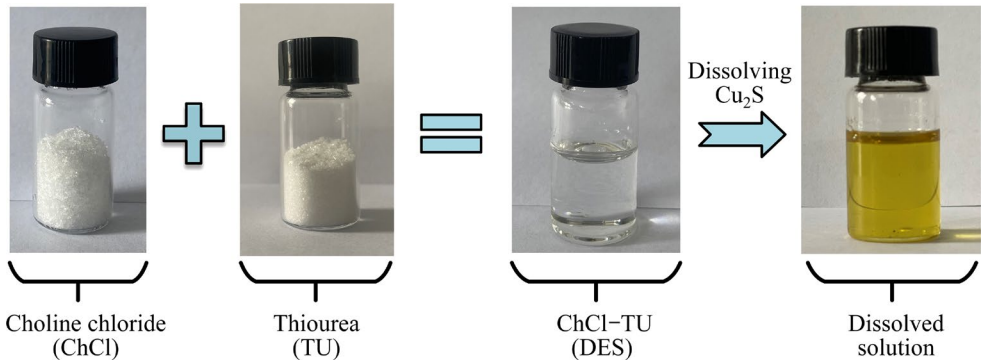

Fig. 1 Schematic of dissolution of Cu_2S in ChCl−TU DES

3 Results and discussion

3.1 Electrochemical behavior

To investigate the possibility of Cu_2S reduction to metallic Cu and to determine a more suitable initial potential for subsequent tests, CV was performed on the electrode, both without and with 0.02 mol/L Cu_2S, at a scan rate of 50 mV/s and a temperature of 80 °C. Figure 2 presents the results of these investigations.

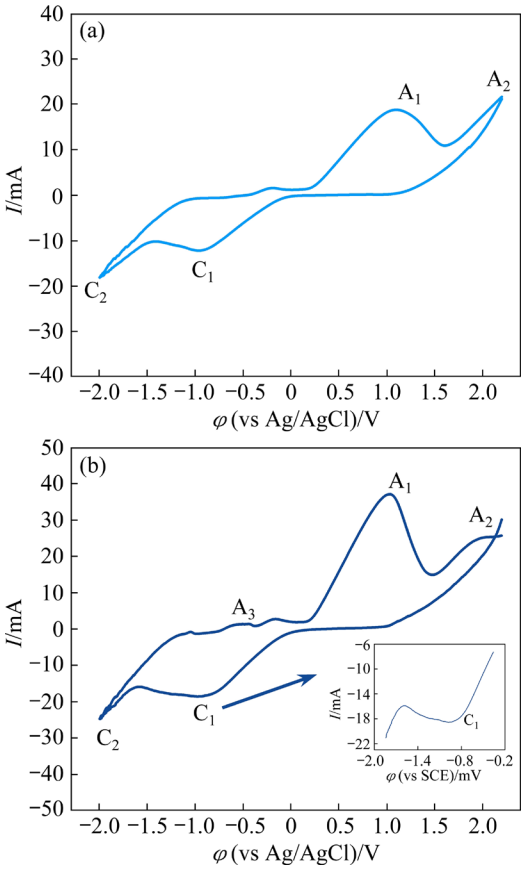

Fig. 2 Cyclic voltammetry plots of ChCl−thiourea (TU) DES (a) and ChCl−TU with 0.02 mol/L Cu_2S (b)

Initially, the cathodic scan ranged from 2.2 to −2.0 V, followed by the anodic scan from −2.0 to 2.2 V. When the potential dropped below −1.45 V, the cathodic current increased rapidly, indicating the reduction of ammonium salt (Cat^+) [23]. Conversely, when the potential exceeded 1.6 V, the anodic current was attributed to the oxidation of Cl^-, corresponding to Reaction (3). The peak areas of the redox peaks A_1/C_1 were nearly identical, which were ascribed to the oxidative decomposition and reduction of thiourea corresponding to Reactions (1) and (2), respectively [24]. Upon adding 0.02 mol/L Cu_2S to ChCl−TU, one anodic peak A_3 emerged, and the cathodic peak current of C_1 was greater than that in Fig. 2(a). This indicated that the new anodic peak A_3 could be attributed to the stripping of Cu to Cu^+, corresponding to Reaction (4). Additionally, the peak area of A_1 significantly exceeded that of C_1 in Fig. 2(b), and the current value of peak A_1 was higher than that in Fig. 2(a). This observation could be attributed to the oxidation of S^{2-} corresponding to Reaction (5) [25], which may be encompassed within A_1:

$$2SC(NH_2)_2 = [(SCN_2H_4)_2]^{2+} + 2e \quad (1)$$

$$[(SCN_2H_4)_2]^{2+} + 2e = 2SC(NH_2)_2 \quad (2)$$

$$2Cl^- = Cl_2 + 2e \quad (3)$$

$$Cu + 2Cl^- - e = [CuCl_2]^- \quad (4)$$

$$S^{2-} = S + 2e \quad (5)$$

To determine the electrolysis voltage, a cell-voltage test was performed. As shown in Fig. 2(b), a new anodic peak A_3 appeared after the dissolution of Cu_2S. At this point, the reduction peak C_3 corresponding to A_3 could also be encompassed within the C_1 peak. It was not feasible to ascertain the reduction potential of Cu^+ based solely on anodic peak A_3. Consequently, a more negative potential was selected for electrolysis to test the cell voltage, which could reduce Cu^+ to Cu. Finally, the cell voltage was measured to be 0.9 V.

3.2 Effect of electrolysis voltage on deposit morphology

Cell voltage is one of the most influential parameters in electrolysis and it is important to select an appropriate cell voltage. Based on this, the constant voltage electrodeposition was performed in ChCl−TU with a concentration of 0.02 mol/L Cu_2S at various electrolysis potentials ranging from 0.7 to 1.2 V. The constant voltage electrolysis was performed at 80 °C for 2 h.

The morphologies of the cathodic products after electrolysis at different voltages were observed using SEM (Figs. 3(a−e)). At the voltages of 0.7−1.2 V, the electrodeposited cathodes produced consisted of spherical nodules with homogenous particles and the size and number of spherical particles tended to increase with increasing voltage. In particular, the resulting deposits obtained at 0.9 and 1.0 V showed a highly porous structure consisting of well-organized nanosheets. The densest

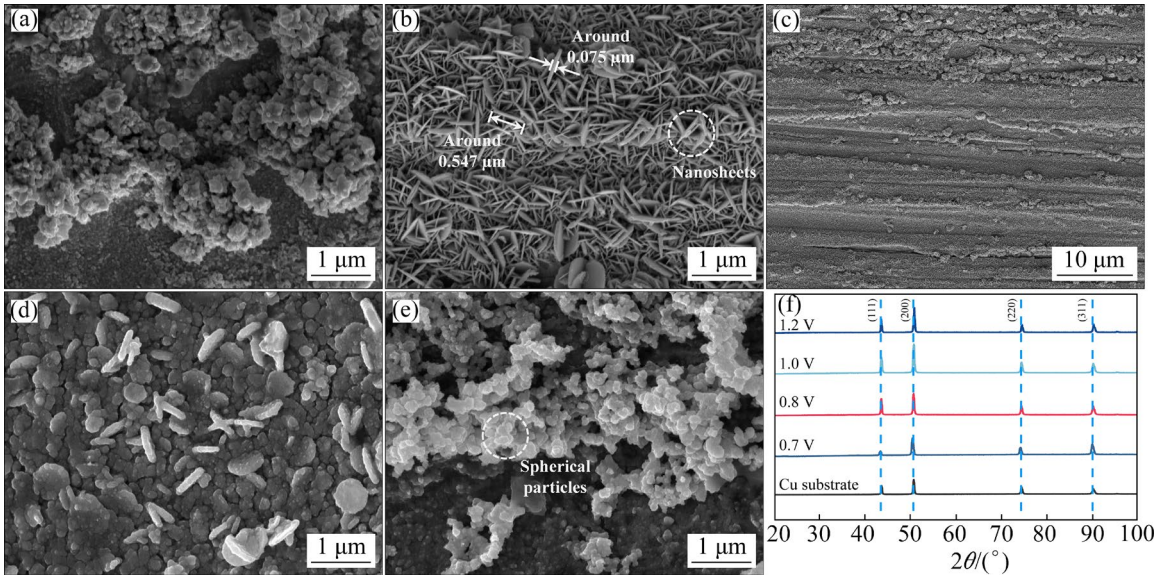

Fig. 3 Microscopic morphology and phase characterization of electrolysis products at different voltages (temperature: 80 °C; time: 2 h) in ChCl−TU DES: (a) 0.7 V; (b, c) 0.9 V; (d) 1.0 V; (e) 1.2 V; (f) XRD patterns of cathodic products

and thinnest nanosheet morphologies were obtained at a voltage of 0.9 V. The nanosheet deposits from ChCl−TU appeared to have a two dimensional morphology, perpendicular to the substrate, and the crystallites retained the hexagonal structure usually found in metal deposits. However, this appeared to inhibit the growth on specific crystal faces, leading to the observed morphology. This nanosheet morphology was attributed to specific chloride adsorption at the growing Cu surface. The only Cu species in ChCl−TU was $[CuCl_2]^-$, and when $[CuCl_2]^-$ was reduced at the electrode surface, the Cl^- was discharged. This chloride adsorption onto the growing Cu surface inhibited the adsorption of $[CuCl_2]^-$ onto the electrode surface. Moreover, the high chloride activity of the ChCl−TU DES resulted in large amounts of chloride adsorption [26]. ABBOTT et al [27] and CVETKOVIĆ et al [28] separately prepared zinc and aluminum deposits with similar sheet-like morphologies in ChCl−EG−$ZnCl_2$ and $AlCl_3$−urea, respectively.

XRD patterns of the Cu electrodeposits on Cu substrate obtained at 80 °C for 2 h with different electrolysis voltages are shown in Fig. 3(f). It could be seen that the deposits were all metallic Cu and the peaks corresponding to the XRD spectra were (111), (200), (220) and (311) crystalline planes from left to right, which were face-centered cubic (FCC) structures. In all the XRD patterns, the crystallites were preferentially oriented in the (200) plane, which was epitaxially grown on a Cu substrate [29], while the oriented (111) planes were parallel to the Cu substrate [30]. The intensity of the diffraction peaks of the (111) and (200) planes gradually increased with increasing deposition potential, and the corresponding deposits grew along the Cu substrate and epitaxially. However, at the potential of 1.2 V, the diffraction peaks of the (111) and (200) planes decreased. If the nanosheets grew too large in the epitaxial direction, they would grow in the direction parallel to the substrate. At this point, the thickness of the nanosheets increased, and the number of nanosheets parallel to the substrate growth direction also increased.

3.3 Effect of electrolysis temperature on deposit morphology

A suitable temperature during electrolysis is crucial for metal preparation and extraction from DES. The surface morphologies of the cathodic product electrodeposited from ChCl−TU with 0.02 mol/L Cu_2S at different temperatures are shown in Fig. 4 and the temperature ranges from 75 to 90 °C. The constant voltage electrolysis measures were performed at a potential of 0.9 V for 2 h. As shown in Figs. 4(a−e), the cathodic electrodeposits produced at different temperatures were composed of well-organized nanosheets. The size of the nanosheets gradually increased with increasing temperature. When the temperature was 80 °C, the obtained nanosheet deposits were denser, thinner,

and more compact than those prepared at other temperatures. The XRD patterns of the Cu nanosheet deposits prepared at different temperatures are shown in Fig. 4(f) and are consistent with the previous results, showing possible peaks of Cu in Fig. 3(f). The preferential orientation of the deposited nanosheets was the (200) crystalline plane at different temperatures. The intensity of the diffraction peaks of the (111) and (200) planes gradually increased upon the commencement of electrolysis, consistent with Fig. 3(f). The nanosheet deposits initially grew in the epitaxial direction until the epitaxial growth becomes excessive. Then, the increase of the (200) surface shows down, while the (111) surface increases further, and the growth direction shifts to become parallel to the Cu substrate.

3.4 Effect of electrolysis time on deposit morphology

Figures 5(a−e) present the morphology of the cathodic electrodeposits at various electrolysis time

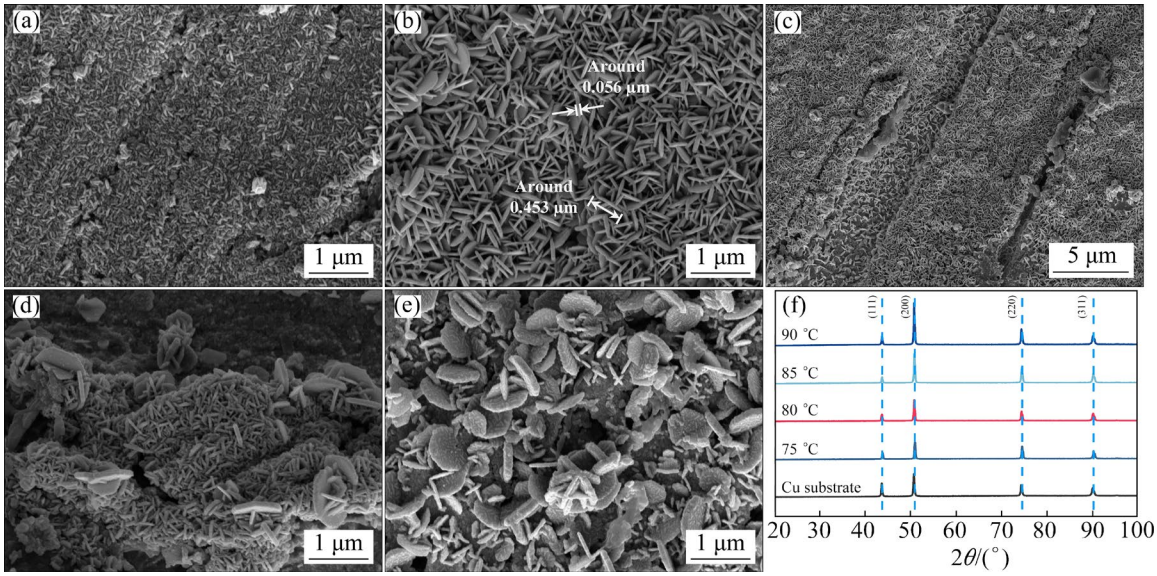

Fig. 4 Microscopic morphology and phase characterization of electrolysis products at various temperatures (electrolysis voltage: 0.9 V; time: 2 h) in ChCl−TU DES: (a) 75 °C; (b, c) 80 °C; (d) 85 °C; (e) 90 °C; (f) XRD patterns of cathodic products

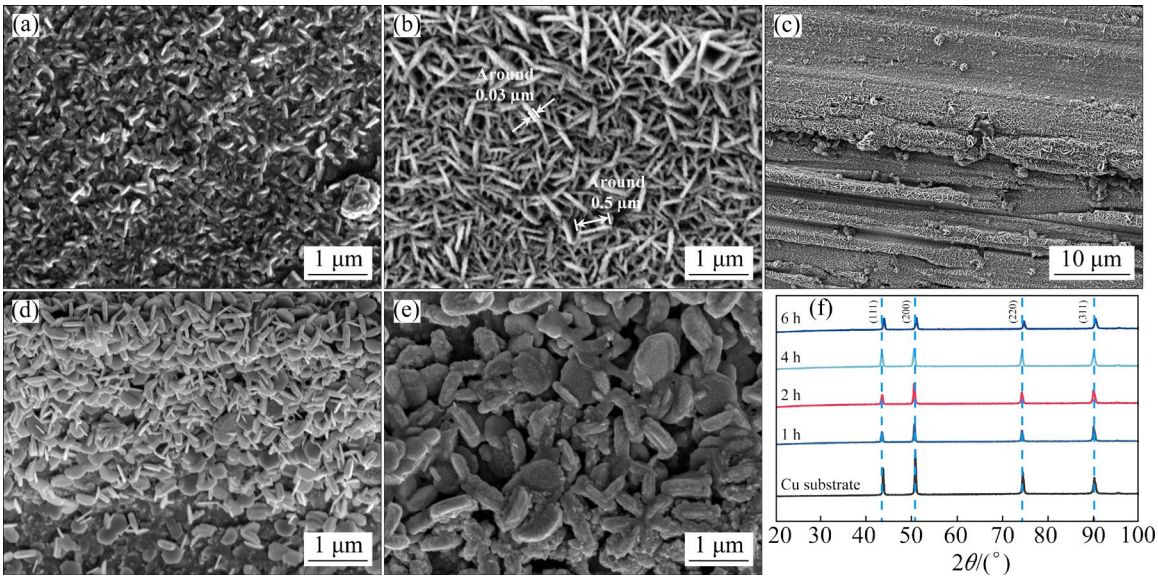

Fig. 5 Microscopic morphology and phase characterization of electrolysis products at different time (electrolysis voltage: 0.9 V; temperature: 80 °C) in ChCl−TU DES: (a) 1 h; (b, c) 2 h; (d) 4 h; (e) 6 h; (f) XRD patterns of cathodic products

ranging from 1 to 6 h, and the electrolysis was performed at 0.9 V and 80 °C. The corresponding XRD patterns of the deposits are shown in Fig. 5(f). With increasing electrolysis time, the size and thickness of the nanosheets gradually increased and decreased, respectively. The proportion of nanosheets grown perpendicular to the Cu substrate decreased as the nanosheet size increased, because the dominance of the oriented (200) plane growing epitaxially on the substrate gradually decreased with increasing time. Instead, the orientation of the (111) plane along the substrate gradually increased. When the electrolysis time was 6 h, the thickness of the nanosheet deposits reached its maximum value. The densest and thinnest nanosheet morphologies were obtained at an electrolysis time of 2 h.

3.5 Constant voltage electrolysis

The phase compositions and morphologies of the electrolysis products were characterized, as shown in Fig. 6. Based on the previous results, we conducted constant voltage electrolysis at 80 °C and 1.2 V for 6 h. Characterization of the cathodic product is presented in Figs. 6(a, b, d), revealing that dense nanosheets with a length of approximately 500 nm and a thickness of approximately 30 nm were obtained. The SEM−EDS (Fig. 6(a)), XRD (Fig. 6(b)), and XPS (Fig. 6(d)) patterns confirmed that the cathodic product was metallic copper. The XRD spectra indicated crystalline planes of (111), (200), (220), and (311), all of which were face-centered cubic (FCC) structures, with the optimal crystalline plane being (200).

In the XPS spectrum of the cathodic product, two main Cu 2p core-level peaks were observed at 932.45 and 951.80 eV, corresponding to Cu $2p_{3/2}$ and Cu $2p_{1/2}$. Additionally, two satellite peaks were observed at higher binding energies (942.91 and 962.34 eV), indicating a partially filled d-block ($3d_9$) of Cu^{2+} ions [31].

SEM−EDS images of the anodic products are shown in Fig. 6(c). SEM images show uniformly sized particles and the size of the particles was approximately 10 μm. The EDS spectrum revealed S peaks, indicating that the anodic product was composed of monolithic sulfur.

Figure 7(a) shows the current–time (I–t) curve for the Cu_2S electrolysis process at 0.9 V and 80 °C for 6 h. Upon applying a voltage, the current rapidly

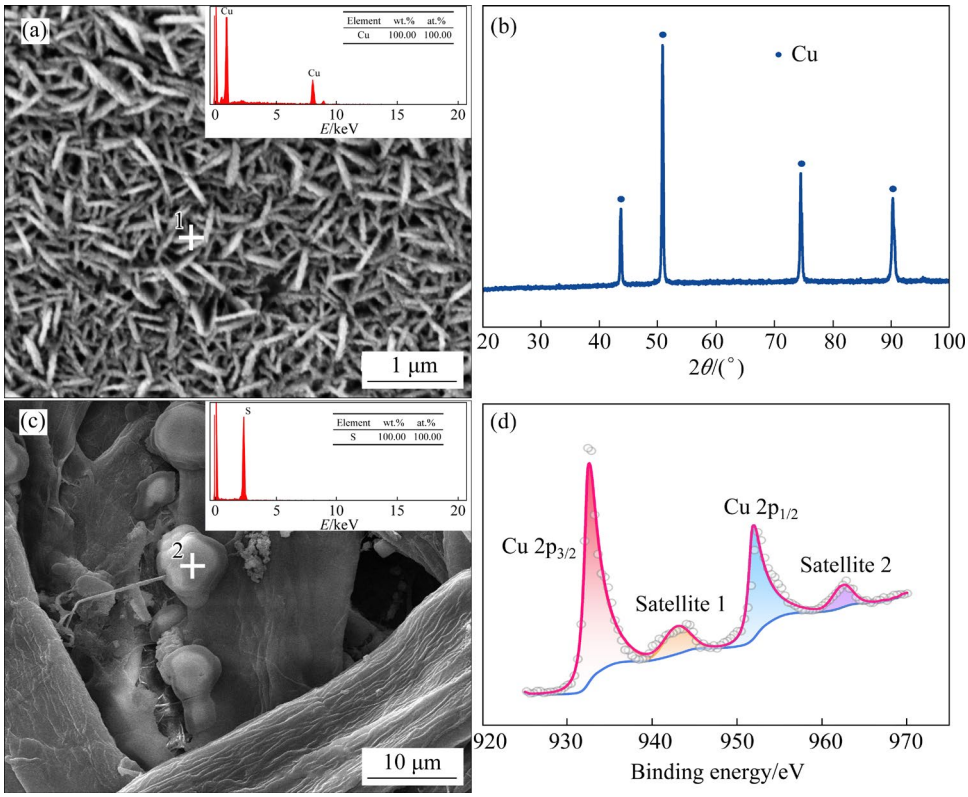

Fig. 6 Microscopic morphology and phase characterization of electrolysis products: (a) SEM−EDS results of cathodic products; (b) XRD pattern of cathodic products; (c) SEM−EDS results of anodic products; (d) XPS spectra of cathodic products

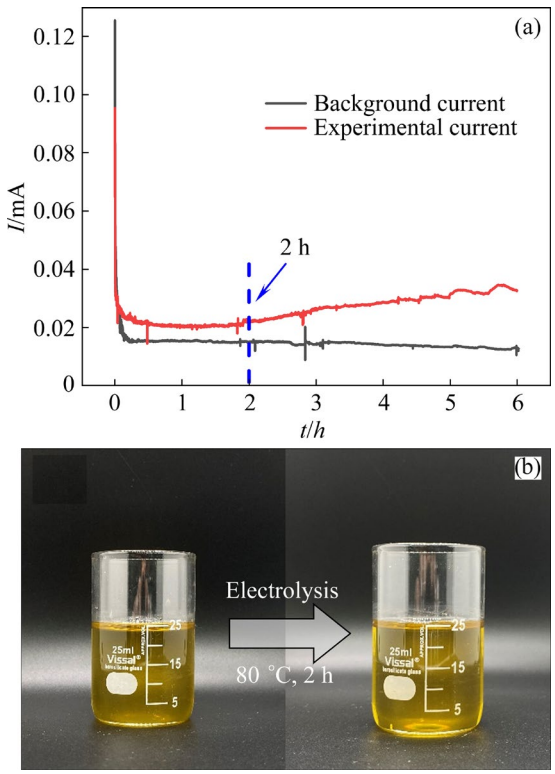

Fig. 7 Variations of cathodic current with electrodeposition time in ChCl−TU−Cu_2S at 0.9 V and 80 °C for 6 h (a); Color change of electrode before and after electrolysis (b)

increased from 0, which was attributed to the rapid reduction and nucleation of $[CuCl_2]^-$ on the copper substrate at the initial stage. Subsequently, the current rapidly decreased, which could be attributed to the decrease in the concentration of $[CuCl_2]^-$ ions surrounding the electrode as they were reduced to elemental Cu. During the reduction of $[CuCl_2]^-$ to Cu, the contact resistance between the electrode and the electrolyte relatively increased. As time progressed, the current gradually changed insignificantly forming a plateau region indicating that reduction of $[CuCl_2]^-$ reached equilibrium. Finally, the current steadily decreased as the electrolysis time approached approximately 2 h, likely because the raw materials were reduced to Cu, resulting in a decrease in the current. The color changes of ChCl−TU−Cu_2S before and after electrolysis are shown in Fig. 7(b). The color of the electrolyte changed insignificantly from yellow to pale yellow. Regarding the background current curve, the current exhibited stability and was lower than the experimental current. After 6 h of electrolysis, the electrolyte exhibited no observable alteration in color and retained its original white and transparent appearance. The anodic products were obtained by electrolyte washing and filtration. Furthermore, the phase compositions and morphologies of the anodic electrolysis products were characterized. However, no distinctive peaks or images corresponding to sulfur particles were detected.

To further estimate the superior performance in terms of specific surface area of the Cu nanosheet deposits, the electrochemically active surface area (ECSA) was calculated. This calculation was based on the electrochemical double-layer capacitance (C_{dl}) using cyclic voltammetry (CV) at different scan rates, as shown in Figs. 8(a, b). The calculation followed the proportionality between ECSA and C_{dl}, based on the equation ECSA=C_{dl}/C_s. Here, C_s represents the specific capacitance, which is valued at 40 μF/cm^2 in 0.1 mol/L KOH electrolyte [32]. The values of C_{dl} were extracted from the slope of the current density plotted as a function of scan rate, as shown in Fig. 8(c). The C_{dl} values for Cu substrate and Cu nanosheet deposits were 0.8 and 1.35 mF/cm^2, respectively. As shown in Fig. 8(d), the calculated ECSA of the Cu nanosheet deposits was 34 cm^2, which was higher than that of the Cu substrate (20 cm^2). A large specific surface area is beneficial for electrocatalytic performance in electrochemical water splitting.

3.6 Electrolysis mechanism

To provide a clearer interpretation of the underlying mechanism, the DES before and after dissolving Cu_2S was analyzed. Figure 9(a) shows the FT-IR spectra illustrating the standard stretching and bond vibration IR frequencies of the different functional groups of the ChCl−TU DES with and without Cu_2S. The vibrational bands at 3262 and 3155 cm^{-1} corresponded to the symmetric stretching and bending vibrations of NH_2 [33]. However, the vibrational band at 3100−3500 cm^{-1} was broader than the other vibrational bands, which indicated the formation of hydrogen bonds [34]. Moreover, the band at 948 cm^{-1} indicated that the structure of Ch^+ was not destroyed in the ChCl−TU DES [35]. The bands at 1604, 1463, and 1077 cm^{-1} were attributed to the symmetric stretching vibration of C═S, C—N, and C—N, respectively [36]. The peak at 724 cm^{-1} corresponded to the stretching vibration of C═S [37].

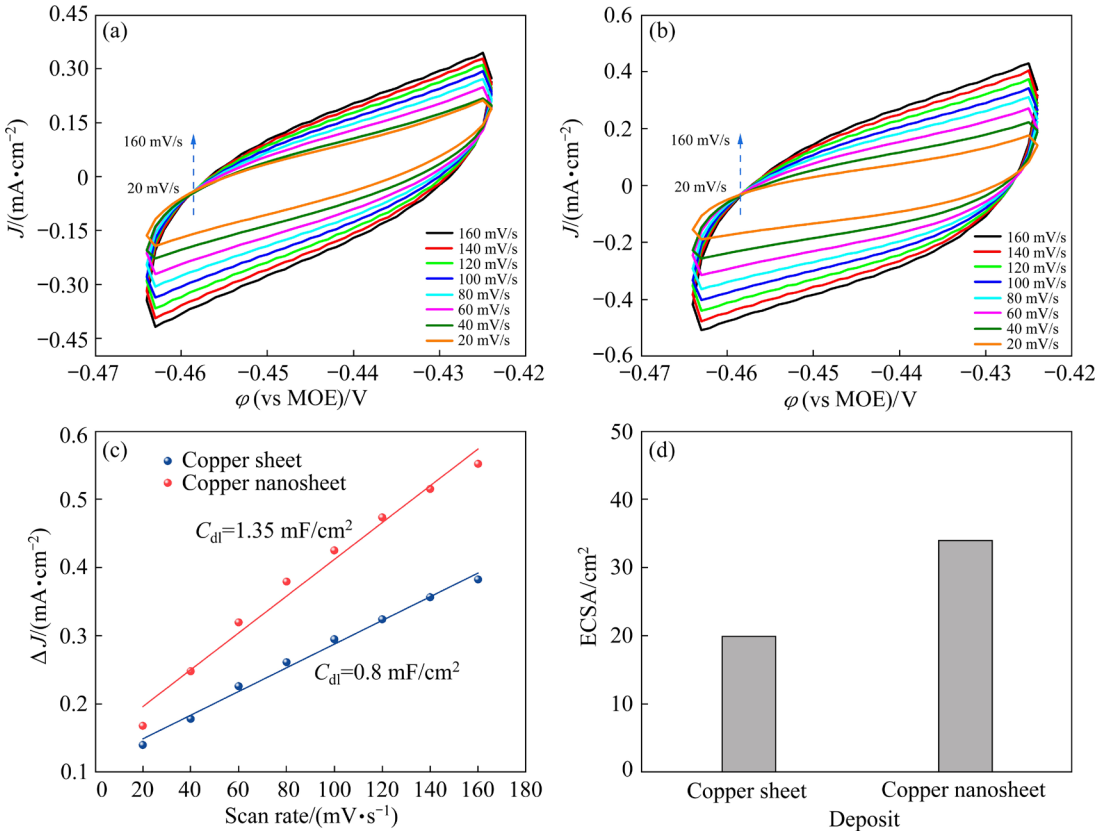

Fig. 8 Double-layer capacitance measurements of determining electrochemically active surface area (ECSA) for Cu sheet in 1 mol/L KOH: (a) Before deposition; (b) After deposition; (c) Corresponding linear fitting of ΔJ versus scan rate; (d) ECSA values for Cu sheet before and after deposition

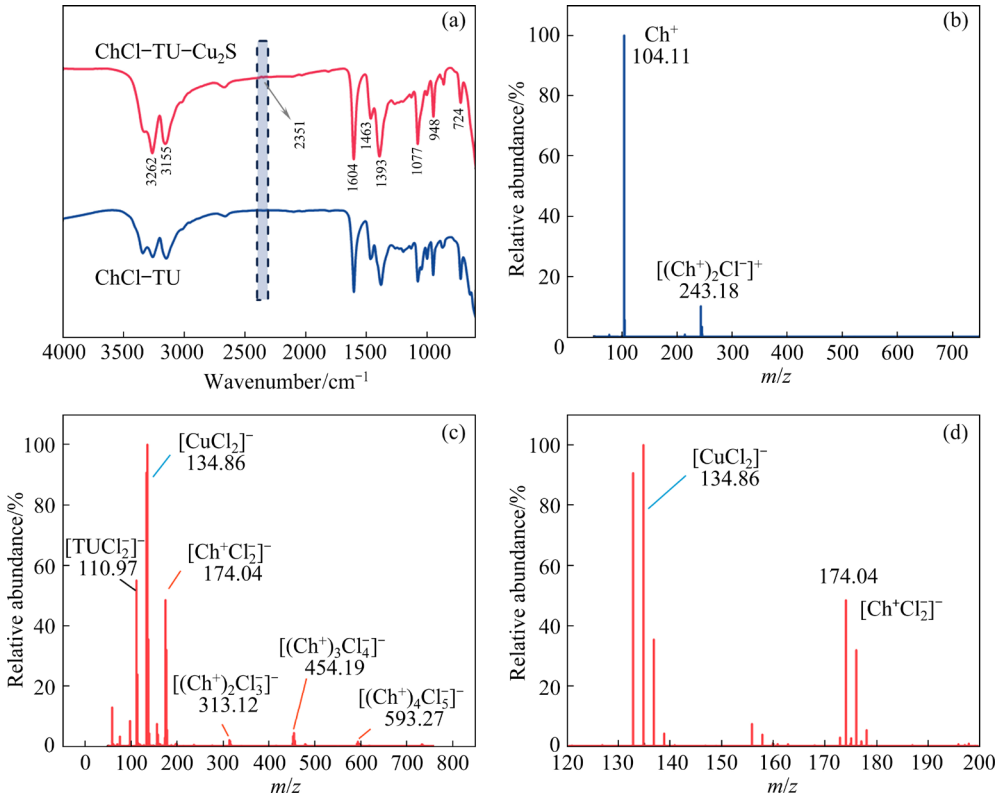

Fig. 9 FT-IR results of ChCl−TU DES without and with 0.02 mol/L Cu_2S (a); ESI-MS results of ChCl−TU DES with 0.02 mol/L Cu_2S in positive mode (b) and negative mode (c); Partial magnification (d) of (c)

Upon adding Cu_2S, a new absorption peak emerged at 2351 cm^{-1}, while the intensity of the other peaks remained relatively unchanged, suggesting the formation of a complex anion. To further substantiate these findings, ESI-MS analyses of ChCl−TU−Cu_2S were performed (Figs. 9(b−d)). In the positive mode, the main components were Ch^+ and the complex anion $[Ch_2Cl]^+$. In the negative mode, the dominant species were $[(Ch^+)_n(Cl^-)_{n+1}]^-$ (n≥1) ion pairs formed by the combination of Ch^+ and Cl^-. This further confirmed that the Ch^+ structure remained intact in the ChCl−TU DES. A new peak at m/z=134.86 was attributed to $[CuCl_2]^-$, indicating that Cu_2S dissolved as $[CuCl_2]^-$ upon addition to ChCl−TU, consistent with the FT-IR results.

Figure 10 shows a schematic of electrolytic deposition conducted at 0.9 V and 80 °C for 6 h. As the electrolysis time increased, the obtained diagram could be divided into five stages. At the beginning of electrolysis, Cu was deposited on the substrate in the form of nanowires. Subsequently, the nanowires grew in an interlaced manner and expanded on the substrate surface, with a tendency to evolve into nanosheets. The nanosheets were then interlaced over the entire substrate, after which they grew epitaxially along the substrate. Finally, the nanosheets grew radially again, at which the nanosheets were thicker and thicker.

In this study, a one-step separation and recovery process for Cu and sulfur from Cu_2S was proposed, as illustrated in Fig. 11(a). The anodic and cathodic reactions for the separation and recovery electrolysis processes are shown in Eqs. (6)−(9):

Dissolution reaction:

$$Cu_2S+4Cl^-=2[CuCl_2]^-+S^{2-} \quad (6)$$

Anode reaction:

$$S^{2-}-2e=S \quad (7)$$

Cathode reaction:

$$[CuCl_2]^-+e=Cu+2Cl^- \quad (8)$$

Overall reaction:

$$Cu_2S=2Cu+S \quad (9)$$

In the ChCl−TU DES, Cu nanosheets were deposited on the cathodic substrate (Fig. 11(b)) by constant-voltage electrolysis, and sulfur particles were recovered at the anode without SO_2 emission (Fig. 11(a)). After the metal—sulfur bonds were broken down, the metal ions leached out from the sulfide and formed complex anions with chloride ions, which were then reduced to metal monomers, while S^{2-} gave electrons to the electrode and was converted to sulfur monomers. Based on this, a mechanism diagram of the electrolysis of Cu_2S in ChCl−TU DES was proposed (Fig. 11(c)). This process differed from the electrolysis of metal sulfides in molten salts, which was conducted at elevated temperatures and was accompanied by sulfur dioxide emissions. Unlike electrochemical

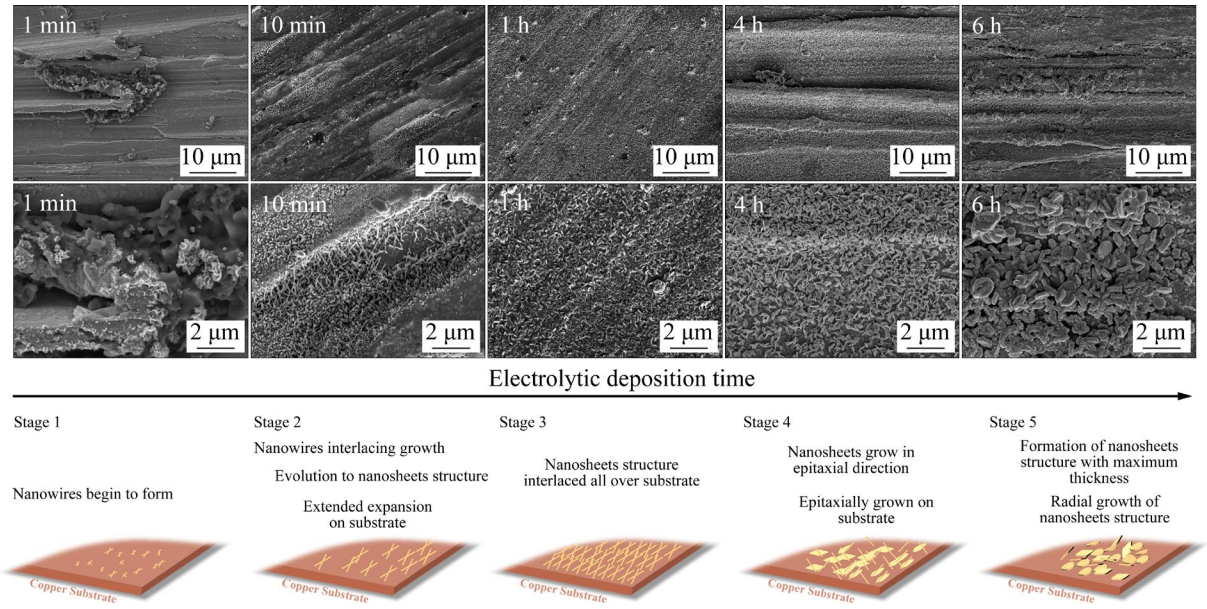

Fig. 10 Schematic of electrochemical growth of copper nanosheets in ChCl−TU DES

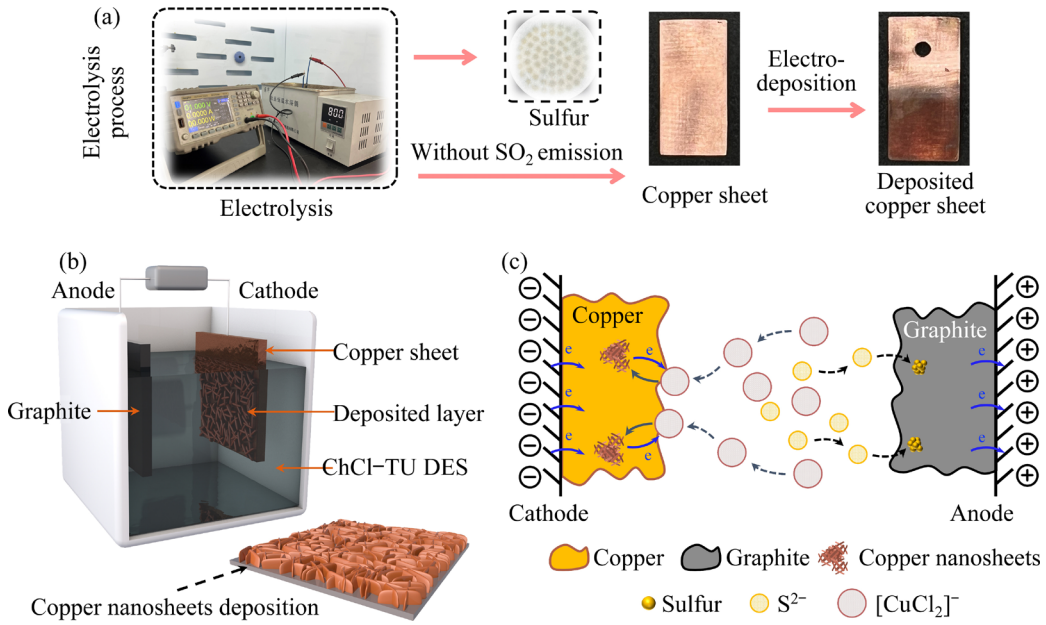

Fig. 11 Schematic of Cu_2S electrolysis in ChCl−TU DES: (a) Flowchart of Cu_2S electrolysis process; (b) Cu_2S electrolysis system in ChCl−TU DES; (c) Mechanism of Cu_2S electrolysis on cathode and anode

oxidation in DES [38], metal sulfides were directly dissolved in DES for one-step separation and recovery, avoiding electromigration after electrochemical oxidation on the anode. Hence, the combination of high efficiency, energy savings, and a short process without SO_2 emissions enabled a straightforward and clean electrochemical metal sulfide separation and recovery process.

4 Conclusions

(1) Optimized conditions of 0.9 V, 80 °C, and a 2 h duration yielded pure copper nanosheet deposits with a length of approximately 500 nm and a thickness of approximately 30 nm, along with sulfur particles of approximately 10 μm in size.

(2) The electrolysis potential significantly influenced the cathodic morphology. At voltages of 0.7 and 1.2 V, the electrodeposited cathodes comprised spherical nodules with homogeneous particles. Notably, the deposits obtained at 0.9 and 1.0 V exhibited a highly porous structure composed of well-organized nanosheets.

(3) Upon adding Cu_2S into ChCl−TU, it dissolved $[CuCl_2]^-$ without disrupting the structure of the choline ion (Ch^+). With increasing electrolysis time, Cu was initially deposited on the substrate in the form of nanowires. Subsequently, the Cu deposition changed from wire to sheet growth, with the growth direction changing from radial to epitaxial along the substrate and back to radial growth.

CRediT authorship contribution statement

Ji-hua LI: Conceptualization, Methodology, Writing − Review & editing; **Jin-feng ZHOU:** Investigation, Data curation; **Wei-jia CHEN:** Software; **Shi-wei HE:** Conceptualization, Funding acquisition, Writing − Review & editing; **Zhong-sheng HUA:** Supervision; **Shi-liang CHEN:** Supervision; **Hui KONG:** Conceptualization.

Declaration of competing interest

The authors declare that they have no known competing financial interests or personal relationships that could have appeared to influence the work reported in this paper.

Acknowledgments

The authors gratefully acknowledge the financial support from the National Natural Science Foundation of China (Nos. 51904005, 52304362), the Key Research Foundation of University in Anhui Province, China (No. 2023AH051113), the Key Laboratory of Ionic Rare Earth Resources and Environment, Ministry of Natural Resources, China (No. 2022IRERE203), and the Distinguished Young Research Project of Anhui Higher Education Institution, China (No. 2023AH020017).

References

[1] QU J, CHEN X, XIE H, GAO S, WANG D, YIN H. Anode electrolysis of sulfides [J]. Proceedings of the National Academy of Sciences, 2022, 119(31): e2202884119−e2202884125.

[2] ZIMMERMAN J B, ANASTAS P T, ERYTHROPEL H C, LEITNER W. Designing for a green chemistry future [J]. Science, 2020, 367(6476): 397−400.

[3] PATELI I M, THOMPSON D, ALABDULLAH S S, ABBOTT A P, JENKIN G R, HARTLEY J M. The effect of pH and hydrogen bond donor on the dissolution of metal oxides in deep eutectic solvents [J]. Green Chemistry, 2020, 22: 5476−5486.

[4] ANGGARA S, BEVAN F, HARRIS R C, HARTLEY J M, FRISCH G, JENKIN G R, ABBOTT A P. Direct extraction of copper from copper sulfide minerals using deep eutectic solvents [J]. Green Chemistry, 2019, 21: 6502−6512.

[5] ABBOTT A P, BARRON J C, RYDER K S. Electrolytic deposition of Zn coatings from ionic liquids based on choline chloride [J]. Transactions of the IMF, 2009, 87(4): 201−207.

[6] ABBOTT A P, EL TTAIB K, RYDER K S, SMITH E L. Electrodeposition of nickel using eutectic based ionic liquids [J]. Transactions of the IMF, 2008, 86(4): 234−240.

[7] ABBOTT A P, AZAM M, FRISCH G, HARTLEY J, RYDER K S, SALEEM S. Ligand exchange in ionic systems and its effect on silver nucleation and growth [J]. Physical Chemistry Chemical Physics, 2013, 15(40): 17314−17323.

[8] ABBOTT A P, HARRIS R C, HSIEH Y T, RYDER K S, SUN I W. Aluminium electrodeposition under ambient conditions [J]. Physical Chemistry Chemical Physics, 2014, 16(28): 14675−14681.

[9] CHEEK G T, O'GRADY W E, EL ABEDIN S Z, MOUSTAFA E M, ENDRES F. Studies on the electrodeposition of magnesium in ionic liquids [J]. Journal of the Electrochemical Society, 2007, 155(1): D91−D95.

[10] ABBOTT A P, CAPPER G, DAVIES D L, RASHEED R K. Ionic liquid analogues formed from hydrated metal salts [J]. Chemistry−A European Journal, 2004, 10(15): 3769−3774.

[11] LIU A, SHI Z, REDDY R G. Electrodeposition of zinc from zinc oxide in 2:1 urea/1-butyl-3-methylimidazolium chloride ionic liquid [J]. Journal of the Electrochemical Society, 2017, 164(9): D666−D673.

[12] YANG H, REDDY R G. Electrochemical deposition of zinc from zinc oxide in 2: 1 urea/choline chloride ionic liquid [J]. Electrochimica Acta, 2014, 147: 513−519.

[13] TANG J, LV D, XU C, HUA Y, ZHANG Q, NIU P, ZHU X. The effect of water on the tin electrodeposition from [Bmim]HSO_4 ionic liquid [J]. International Journal of Electrochemistry, 2018, 2018: 1−7.

[14] LIU A, SHI Z, REDDY R G. Electrodeposition of Pb from PbO in urea and 1-butyl-3-methylimidazolium chloride deep eutectic solutions [J]. Electrochimica Acta, 2017, 251: 176−186.

[15] YANG H, REDDY R G. Fundamental studies on electrochemical deposition of lead from lead oxide in 2:1 urea/choline chloride ionic liquids [J]. Journal of The Electrochemical Society, 2014, 161(10): D586−D592

[16] XIE X, ZOU X, LU X, ZHENG K, CHENG H, XU Q, ZHOU Z. Voltammetric study and electrodeposition of Cu from CuO in deep eutectic solvents [J]. Journal of the Electrochemical Society, 2016, 163(9): D537−D543.

[17] ABBOTT A P, AL-BASSAM A Z, GODDARD A, HARRIS R C, JENKIN G R, NISBET F J, WIELAND M. Dissolution of pyrite and other Fe−S−As minerals using deep eutectic solvents [J]. Green Chemistry, 2017, 19(9): 2225−2233.

[18] WANG Z, RU J, BU J, HUA Y, ZHANG Y, XU C. Direct electrochemical desulfurization of solid Sb_2S_3 to antimony powders in deep eutectic solvent [J]. Journal of the Electrochemical Society, 2019, 166(14): D747−D754.

[19] WANG Z, LI Z, BU J, RU J, HUA Y, WANG D. One-step direct desulfurization of cuprous sulfide for copper recovery via electrolysis in deep eutectic solvent [J]. Separation and Purification Technology, 2022, 303: 122133−122142.

[20] GUO M W, SUN C B, YANG W Q, CHEN L, LEI H, ZHANG Q B. Sulphur-induced electrochemical synthesis of manganese nanoflakes from choline chloride/ethylene glycol-based deep eutectic solvent [J]. Electrochimica Acta, 2020, 341: 136017−136015.

[21] WANG J, WANG P, WANG Q, MOU H, CAO B, YU D, WANG D, ZHANG S, MU T. Low temperature electrochemical deposition of aluminum in organic bases/thiourea-based deep eutectic solvents [J]. ACS Sustainable Chemistry & Engineering, 2018, 6(11): 15480−15486.

[22] CHEN T, YING H, ZHANG C, BI J, LI Z, HAO J. Engineering an Fe_2O_3/FeS hybrid catalyst from a deep eutectic solvent for highly efficient electrocatalytic N_2 fixation [J]. Chemical Communications, 2021, 57(54): 6688−6691.

[23] WANG T, GAO H, JIN X, CHEN H, PENG J, CHEN G. Electrolysis of solid metal sulfide to metal and sulfur in molten NaCl−KCl [J]. Electrochemistry communications, 2011, 13(12): 1492−1495.

[24] YUE D, JIA Y, YAO Y, SUN J, JING Y. Structure and electrochemical behavior of ionic liquid analogue based on choline chloride and urea [J]. Electrochimica Acta, 2012, 65: 30−36.

[25] MENG D, FENG Z, YANG J, WANG M, XIA C, ZHAO Y, XU Y, HUANG X. Reaction between Ce^{4+} ion and thiourea in aqueous HCl medium: An electrochemical study [J]. Journal of the Electrochemical Society, 2021, 168(10): 103502−103506.

[26] ABBOTT A P, BARRON J C, FRISCH G, RYDER K S, SILVA A F. The effect of additives on zinc electrodeposition from deep eutectic solvents [J]. Electrochimica Acta, 2011, 56: 5272−5279.

[27] ABBOTT A P, BARRON J C, FRISCH G, GURMAN S, RYDER K S, SILVA A F. Double layer effects on metal nucleation in deep eutectic solvents [J]. Physical Chemistry Chemical Physics, 2011, 13(21): 10224−10231.

[28] CVETKOVIĆ V, VUKIĆEVIĆ N, JOVIĆEVIĆ N, STEVANOVIĆ J, JOVIĆEVIĆ N. Aluminium electrodeposition under novel conditions from $AlCl_3$−urea deep eutectic solvent at room temperature [J]. Transactions of Nonferrous Metals Society of China, 2020, 30(3): 823−834.

[29] SEAKR R. Microstructure and crystallographic

characteristics of nanocrystalline copper prepared from acetate solutions by electrodeposition technique [J]. Transactions of Nonferrous Metals Society of China, 2017, 27(6): 1423−1430.

[30] LUC W, FU X, SHI J, LV J J, JOUNY M, KO B H, XU Y, TU Q, HU X, WU J, YUE Q, LIU Y, JIAO F, KANG Y. Two-dimensional copper nanosheets for electrochemical reduction of carbon monoxide to acetate [J]. Nature Catalysis, 2019, 2(5): 423−430.

[31] SINGH B P, CHAUDHARY M, KUMAR A, SINGH A K, GAUTAM Y K, RANI S, WALIA R. Effect of Co and Mn doping on the morphological, optical and magnetic properties of CuO nanostructures [J]. Solid State Sciences, 2020, 106: 106296−106304.

[32] LIU G, HE D, YAO R, ZHAO Y, LI J. Amorphous NiFeB nanoparticles realizing highly active and stable oxygen evolving reaction for water splitting [J]. Nano Research, 2018, 11: 1664−1675.

[33] MAHTO B, KHAN A A, BARHOI A, HUSSAIN S. Hierarchical Cu_3BiS_3 nanostructures with thermally controlled morphology for photoconductive, photothermal, and catalytic applications [J]. ACS Applied Nano Materials, 2023, 6(8): 6784−6797.

[34] LI Y, LI Y, CAO C, LI H, FAN X, XU X, ZHU M. Solid-liquid phase change of choline chloride type deep eutectic solvents towards lubrication regime [J]. Journal of Molecular Liquids, 2022, 365: 120162−120173.

[35] LI Y, LI Y, LI H, FAN X, YAN H, CAI M, XU X, ZHU M. Insights into the tribological behavior of choline chloride−Urea and choline chloride−thiourea deep eutectic solvents [J]. Friction, 2023, 11(1): 76−92.

[36] KARIMI M, DADFARNIA S, HAJI SHABANI A M. Hollow fibre-supported graphene oxide nanosheets modified with a deep eutectic solvent to be used for the solid-phase microextraction of silver ions [J]. International Journal of Environmental Analytical Chemistry, 2018, 98(2): 124−137.

[37] MADHURAMBAL G, MARIAPPAN M, RAVINDRAN B, MOJUMDAR S C. Thermal and FTIR spectral studies in various proportions of urea thiourea mixed crystal [J]. Journal of Thermal Analysis and Calorimetry, 2011, 104: 885−891.

[38] BEVAN F, GALEB H, BLACK A, PATELI I M, ALLEN J, PEREZ M, FELDMANN J, HARRIS R, JENKIN G, ABBOTT A, HARTLEY J. A unified method for the recovery of metals from chalcogenides [J]. ACS Sustainable Chemistry & Engineering, 2021, 9(7): 2929−2936.

氯化胆碱–硫脲低共熔溶剂中电解 Cu_2S 制备铜纳米片和硫颗粒

李继华[1]，周金凤[1]，陈唯佳[1]，何世伟[1,2]，华中胜[1,2]，陈世梁[1]，孔 辉[1,3]

1. 安徽工业大学 冶金工程学院，马鞍山 243002；
2. 安徽工业大学 芜湖技术创新研究院，芜湖 241000；
3. 安徽省冶金流程与系统科学国际联合研究中心，马鞍山 243002

摘 要：将 Cu_2S 溶解于氯化胆碱–硫脲(ChCl−TU)低共熔溶剂中电解，同步制备铜纳米片和硫颗粒。在 0.9 V、80 ℃和 2 h 的最优电解条件下，可沉积出长度约为 500 nm、厚度约为 30 nm 的纯铜纳米片，同步生成平均粒径约为 10 μm 的硫颗粒。电解电压显著影响阴极产物的形貌。Cu_2S 在 ChCl−TU 中溶解后，铜以络阴离子$[CuCl_2]^-$的形式存在，胆碱离子(Ch^+)的结构并未被破坏。随着电解时间的延长，铜的沉积由线状逐渐转变为片状生长，生长方向从径向沿基底生长转变为外延生长，然后再回到径向生长。

关键词：硫化亚铜；低共熔溶剂；分离；铜纳米片；电化学回收

(Edited by Bing YANG)